Magnesioreduction Synthesis of Co-Doped beta-FeSi2: Mechanism, Microstructure, and Improved Thermoelectric Properties

Sylvain Le Tonquesse, Zelia Verastegui, Helene Huynh, Vincent Dorcet, Quansheng Guo, Valérie Demange, Carmelo Prestipino, David Berthebaud, Takao Mori, Mathieu Pasturel

Magnesioreduction synthesis of Co-doped β-$FeSi_2$: mechanism, microstructure and improved thermoelectric properties

Sylvain Le Tonquesse,[†] Zelia Verastegui,[†] Hélène Huynh,[‡] Vincent Dorcet,[†] Quansheng Guo,[‡,¶] Valérie Demange,[†] Carmelo Prestipino,[†] David Berthebaud,[‡] Takao Mori,[¶] and Mathieu Pasturel*[,†]

[†]*Univ Rennes, CNRS, ISCR-UMR6226/ScanMAT-UMS2001, F-35000, Rennes, France.*

[‡]*CNRS - Saint-Gobain - NIMS, UMI3629, Laboratory for Innovative Key Materials and Structures (LINK), National Institute for Materials Science, 1-1 Namiki, Tsukuba, Ibaraki 305-0044, Japan.*

[¶]*National Institute for Materials Science (NIMS), WPI-MANA and CFSN, Tsukuba, Japan.*

E-mail: mathieu.pasturel@univ-rennes1.fr

Phone: +33 (0)2 23 23 58 61

Abstract

β-$FeSi_2$ and β-$Co_{0.07}Fe_{0.93}Si_2$ thermoelectric silicides were synthesized from Fe_2O_3 and Si powders using a magnesiothermic process. Detailed study of the reaction mechanism by X-ray diffraction reveals that liquid Mg is mandatory to initiate the reduction. After completion of the reaction in relatively short time (10 h at 1173 K), the magnesiosynthesized iron disilicides are characterized as powders with grain sizes ranging from 30 to 400 nm and containing a high concentration of stacking faults quantified for

the first time using a dedicated refinement software. The thermoelectric properties of spark plasma sintered pellets with submicrometric grain sizes, high stacking fault density and residual micro- to nanoporosities are presented and compared to corresponding materials synthesized by conventional arc-melting process. Strong thermal conductivity reduction of 20 % at 773 K has been achieved thanks to the mesostructuration induced by the magnesioreduction. It results in an improved maximum figure-of-merit ZT reaching 0.18 at 773 K for β-$Co_{0.07}Fe_{0.93}Si_2$.

Keywords

Iron silicide, Thermoelectrics, Magnesiothermy, Mesostructuration, Stacking faults, Thermal conductivity

1 Introduction

Thermoelectric (TE) materials are being extensively investigated because they enable the direct conversion of (wasted) heat into electricity, and *vice versa*, through highly reliable solid state devices.[1,2] The material performances are directly related to the TE figure-of-merit ZT defined as:

$$ZT = \frac{\alpha^2}{\rho(\kappa_L + \kappa_e)}T \quad (1)$$

where α is the Seebeck coefficient, ρ the electrical resistivity, κ_L and κ_e the lattice and electronic contributions to the total thermal conductivity κ and T the absolute temperature. Large enhancement of ZT and subsequent conversion yield is however challenging due to interrelated physical components. Common strategies consist on the one hand in the opti-

mization of the power factor, $PF = \alpha^2/\rho$, essentially *via* doping and band engineering,[3] and on the other hand in the reduction of κ_L *via* nanostructuration, porosity/defects engineering and complex alloying.[4–6] In the past twenty years, these strategies successfully resulted in TE materials with ZT much higher than 1.[7–9] Most of these materials, including clathrates,[10] Pd/Te-based alloys[11] or Hf-containing Heusler phases,[12] are however hardly industrializable candidates because of time and energy consuming syntheses, poor mechanical properties and most importantly chemical compositions including toxic and/or expensive constituents.[13]

From these points of view, β-$FeSi_2$ is considered as a reasonable candidate for large scale application due to its extremely abundant and ecofriendly constituting elements, and good oxidation resistance. However, the intrinsic TE properties of pristine $FeSi_2$ are poor, especially due to its high thermal conductivity (16 - 17 W m^{-1} K^{-1} at 273 K) and electrical resistivity (5 - 10 mΩ m at 370 K).[14] Doping with Co,[14,15] Al,[15] Mn[16] or Cr[14] efficiently improves the maximum ZT to about 0.15. Moreover, the synthesis of β-$FeSi_2$ (space group $Cmce$) by conventional metallurgical routes is facing the peritectoid decomposition in ϵ-FeSi (s.g. $P2_13$) and α-$Fe_{1-\delta}Si_2$ (s.g. $P4/mmm$) above 1255 K,[17] implying long annealing at high-temperature to recover the β-phase. For such reasons, extensive research has been devoted to the development of alternative synthesis routes for nanostructured silicides with reduced thermal conductivity adapted to large scale production. For example, mechanical alloying[14,18–20] or melt spinning[21] followed by reactive sintering were used for the fabrication of mesostructured and highly substituted β-$FeSi_2$. Recently, several studies reported the synthesis of β-$FeSi_2$/Si(Ge) nanocomposites by the eutectoid decomposition of α-$Fe_{1-\delta}Si_2$.[22–25] The resulting microstructure consists in 10 to 200 nm Si(Ge) well-dispersed inclusions inside a β-$FeSi_2$ matrix allowing a κ reduction up to 50 %. Controlled doping remains however difficult by this approach resulting in materials with peak ZT rarely exceeding 0.1,[26–29] but reaching values as high as 0.4 - 0.6 when the doping is successful.[19,25] More exploratory synthesis routes such as laser sintering[30,31] or gas-phase reaction[32] were successful to obtain β-$FeSi_2$ but they still remain more adapted to laboratory scale production.

Sen *et al.* reported an innovative synthesis of (doped) β-$FeSi_2$ nanopowders by magnesioreduction of mixed oxide mixtures prepared by sol-gel method from tetraethylorthosilicate ($Si(OC_2H_5)_3$) and ferric nitrate ($Fe(NO_3)_3{\cdot}9H_2O$).[33,34] The high reducing power of Mg allows the reaction to be carried out in short reaction time (6 h) and at relatively low temperature (1073 K) thus avoiding the post-synthesis annealing step. In addition, the powder obtained by this process has grain sizes as small as 50 nm, which might be suitable for the preparation of nanostructured thermoelectrics. However, the as-reported synthesis procedure remains hardly compatible with industrial scale production, mainly due to the numerous steps involved (up to 6) including a time-consuming preparation of the oxide mixture (2 steps totaling 18 h) from highly hygroscopic reactants.

In the present article, a modified magnesioreduction synthesis for thermoelectric β-$FeSi_2$ and β-$Co_{0.07}Fe_{0.93}Si_2$ powders with 30 - 400 nm grain sizes is described. The preparation of the oxide precursor mixture is realized in a single step by ball-milling (Co-doped) Fe_2O_3 and Si. This offers many advantages such as a higher scalability perspective, the use of cheap, air stable and non-hazardous precursors and a final yield greater than 98 %. The chemical reactivity has been followed by powder X-ray diffraction during the whole process to optimize the temperature/duration of the thermal treatment. The crystal structure, refined for the first time using a dedicated software to analyze the impact of stacking faults on Bragg reflections, and the microstructure, characterized by scanning and transmission electron microscopies, are presented on as-synthesized powders and spark plasma sintered pellets. Finally the improved TE properties are discussed toward the influence of the microstructure and compared to similar materials synthesized by conventional arc-melting/sintering/annealing route.

2 Experimental methods

The experimental set-up for the magnesioreduction synthesis (MR) is described in more details in our previous articles.[35,36] For undoped β-$FeSi_2$, a precursors mixture is first prepared

by dry ball-milling stoichiometric amounts of Fe_2O_3 (Merck, > 99 %) and Si powder (Ventron, 99.9 %) using WC vial and balls (ball-to-powder ratio of 5 : 1) with rotation speed of 650 rpm for 4 h under air atmosphere. Good control of milling conditions of precursors was found essential to prevent contamination by WC during the milling and formation of side-products (FeSi, Fe_3Si, unreacted Si) during the magnesioreduction process. The precursor mixture is cold pressed (100 MPa) in Ø 10 mm pellets with 2 mm height and placed with adequate amount of Mg turnings according to:

$$Fe_2O_3 + 4\,Si + \underset{(+25\%)}{3\,Mg} \longrightarrow 2\,\beta\text{-}FeSi_2 + 3\,MgO$$

in a clamped Mo crucible. The latter is heated under Ar protective atmosphere at a rate of 100 K h^{-1} up to 1173 K, maintained at this temperature for 10 h and cooled down to room temperature by switching off the furnace. The reaction product is recovered by opening the crucible and MgO by-product is removed by soaking the as-synthesized powder twice in diluted hydrochloric acid (2 wt.%) and washing three times with distilled water and once more with ethanol before being dried at 353 K overnight. Densified β-$FeSi_2$ pellets are obtained by spark plasma sintering (SPS, FCT HP-D-10 apparatus) the 'washed' powders in Ø 10 mm graphite dies at 1323 K - 80 MPa for 30 min followed by 24 h annealing at 1100 K in an evacuated silica tube.

For the synthesis of β-$Co_{0.07}Fe_{0.93}Si_2$, the addition of Co_3O_4 to Fe_2O_3 and Si during the ball-milling preparation of the precursor mixture leads to the formation of $CoSi_2$ during the magnesioreduction process, attributed to an uneven distribution of Co in the mixture. Starting from a properly doped $Co_{0.14}Fe_{1.86}O_3$ precursor allows Fe and Co to be homogeneously distributed at the atomic scale and the probability to form side-products is greatly reduced. $Co_{0.14}Fe_{1.86}O_3$ is synthesized by dissolving stoichiometric proportions of $Co(NO_3)_2{\cdot}6H_2O$ (Fluka, $\geq$ 98 %) and $Fe(NO_3)_2{\cdot}9H_2O$ (Fluka, $\geq$ 98 %) in a minimum amount of distilled water and by calcinating the mixture at 773 K for 6 h in air. According to

X-ray diffraction (XRD), the obtained red powder is single phase α-$Co_xFe_{2-x}O_3$ (s.g. $R\bar{3}c$) with $a = 5.0327(1)$ Å and $c = 13.7413(4)$ Å as determined by Le Bail refinement of the diffraction patterns (fig. S1). The lattice parameters are significantly different from those reported for pure α-Fe_2O_3 *(*$a = 5.0368(1)$ Å and $c = 13.7601(3)$ Å[37]) and energy dispersive spectroscopy (EDS) elementary analyses indicate a Co concentration of approximately 2 at.% in agreement with the targeted composition.

The conventional synthesis of β-$FeSi_2$ and β-$Co_{0.07}Fe_{0.93}Si_2$ consisted in arc-melting (AM) stoichiometric amounts of the metallic elements three times to ensure homogenization. The resulting ingots are milled, SPS sintered at 1223 K and 90 MPa for 5 min and finally annealed for 60 h at 1123 K in evacuated silica tubes.

The crystal structure and purity of the samples are checked by powder XRD using a Bruker D8 Advance diffractometer working in the modified Bragg-Brentano geometry with a monochromatized Cu Kα_1 radiation ($\lambda = 1.54059$ Å) and equipped with a LynxEye fast detector. Structural parameters are determined by Rietveld refinements of the XRD patterns using the FullProf or FAULTS softwares[38,39] included in the FullProf Suite package.[40] Scanning electron microscopy (SEM) in secondary and backscattered electrons modes and EDS are performed on a JEOL JSM 7100 F microscope equipped with an Oxford EDS SDD X-Max spectrometer. Transmission electron microscopy (TEM) is performed on a JEOL 2100 LaB_6 instrument operating at 200 kV and equipped with high resolution Gatan US1000 and Orius SC 200D cameras and EDS Oxford 80 mm^2 SDD spectrometer. Preparation of the powder samples for SEM analyses consists in the deposition of powder on carbon tape followed by metallization with carbon while for TEM analyses small amount of the powder is sonificated in absolute ethanol and deposited for drying on a carbon coated copper grid.

The thermal diffusivity (D) is measured by the laser flash analysis (LFA) method on Ø 10 mm and 2 mm thick samples coated with graphite using a Netzsch LFA 467 HyperFlash equipment under N_2 atmosphere. The thermal conductivities are then calculated by the relation $\kappa = D \cdot C_p \cdot d$ with C_p the specific heat of the sample determined thanks to a

Netzsch *Pyroceram* reference and the density d determined by the Archimede method in absolute ethanol. Measurements of the Seebeck coefficient and electrical resistivity are realized simultaneously on 6x2x2 mm^3 bars using a ZEM3 (ULVAC-RIKO Inc., Yokohama, Japan) equipment under He atmosphere.

3 Result and discussion

3.1 Magnesioreduction process

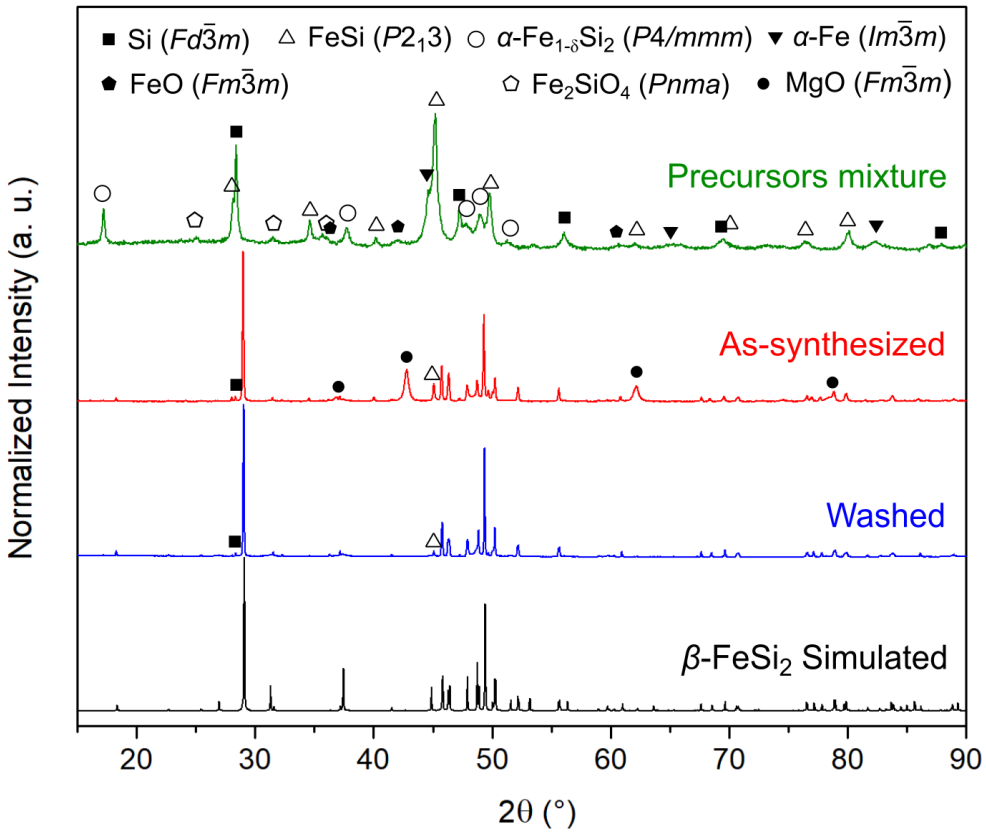

Figure 1: XRD patterns of the precursor mixture (green), as-synthesized (red) and HCl-washed (blue) MR β-$FeSi_2$ powders, as well as simulated pattern for β-$FeSi_2$[41] (black). Intensity discrepancies between some peaks in the experimental and theoretical β-$FeSi_2$ patterns are linked to the presence of (100)[011]/2 stacking faults in the crystals (see text for details).

The XRD pattern of the precursors mixture obtained by ball-milling Fe_2O_3 and Si is

shown in fig. 1. Up to six crystalline phases have been identified indicating a reactive milling. The relative concentrations (mol.%) of the products in the precursors mixture are determined by Rietveld refinement (fig. S2a):

$$Fe_2O_3 + 4\,Si \xrightarrow[4\,h]{650\,rpm} \underset{42\%}{Si} + \underset{23.5\%}{FeSi} + \underset{18\%}{\alpha\text{-}Fe} + \underset{11.5\%}{\alpha\text{-}Fe_{1-\delta}Si_2} + \underset{2.5\%}{FeO} + \underset{2.5\%}{Fe_2SiO_4}$$

Interestingly, Fe^{3+} (Fe_2O_3) is entirely reduced in Fe^{2+} (FeO, Fe_2SiO_4) or metallic Fe (Fe, FeSi, α-$Fe_{1-\delta}Si_2$) during the milling process. Solid state redox reactions occur with Si playing the role of reducing agent most probably according to:

$$2\,Fe_2O_3 + Si \longrightarrow 4\,FeO + SiO_2 \qquad \Delta G_r^\circ(300\ K) = \text{-}353.3\ kJ^{42}$$

$$2\,FeO + Si \longrightarrow 2\,Fe + SiO_2 \qquad \Delta G_r^\circ(300\ K) = \text{-}444.4\ kJ^{42}$$

Both reductions are thermodynamically possible at room temperature in view of their large negative Gibbs free energies. The activation energies are overcome by the highly energetic shocks occurring in the milling vial. Analogous reactions are reported for higher manganese silicides where MnO is reduced by Si in similar milling conditions.[36]

As a result, SiO_2 has to be present in the precursor mixture. Its amorphous nature is suggested by the broad deviation of the background of XRD patterns around 22° associated to silica glass.[43] The Si/Fe atomic ratio of 1.5 determined from Rietveld refinement is much smaller than the value of about 2 expected from the reactant quantities and confirmed by SEM-EDS analyses. A SiO_2 concentration of about 23 mol.% in the precursor mixture can thus be estimated. Moreover, freshly reduced metallic Fe is expected to react with Si by mechanical alloying forming FeSi and α-$Fe_{1-\delta}Si_2$ as already reported in the literature.[18,44,45] The formation of the high temperature allotrope of the disilicide upon milling highlights the

energetic conditions in the vial during the milling. Fe_2SiO_4 is probably formed in a similar manner from FeO and SiO_2. SiO_2, FeO and Fe_2SiO_4 are the remaining oxide phases to be reduced by Mg during the magnesioreduction process.

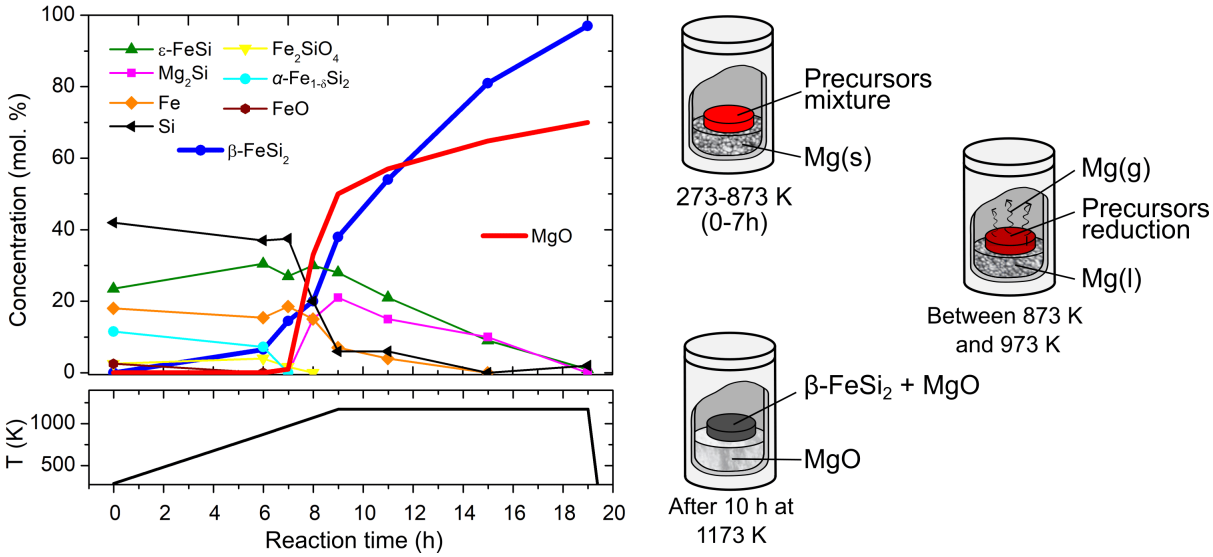

Figure 2: (left) Evolution of the sample composition during the magnesioreduction synthesis of β-$FeSi_2$ determined by Rietveld refinements. The relative deviation on the concentrations is estimated to be well below 5 % according to measurement conditions, quality of the fits and Ref.[46] (right) Schemes of the crucible at three important stages of the reaction: heating-up (top), melting of Mg and reduction of the precursor mixture (middle), completed reaction after 19 h (right) (s: solid, l: liquid, g: gas).

The thermal cycle used for the magnesiothermic reaction consists in a heating ramp up to 1173 K in 9 h followed by a 10 h isothermal plateau. To better understand the reaction mechanism, the reactor was quenched in cold water at different times of the process and the phases in presence were quantified by Rietveld refinement of XRD patterns. The evolution of phase concentrations (excluding MgO) as a function of the reaction time is presented in fig. 2 with lines+symbols while the overall content in MgO in the reaction media is displayed with a red line. The fitted XRD pattern and refined structural parameters and details about the refinement procedure can be found in fig. S2a-h and tables S1-S9.

During the first 6 hours of the reaction, no significant changes can be observed indicating that Mg is quite unreactive below 873 K toward the species in presence. Only α-$Fe_{1-\delta}Si_2$

slowly transforms in β-$FeSi_2$ which is the thermodynamically stable allotrope in this temperature range. Between 873 and 973 K, the reduction process starts as indicated by the formation of MgO (1 mol.%). Interestingly, it corresponds well to the melting temperature of Mg (melting point T_m = 922 K) and suggests that liquid Mg with high vapor pressure (383 Pa at T_m) is required to initiate the reduction.[47] At 1073 K, MgO and newly formed Mg_2Si intermetallic represent as much as 33 and 16 mol.% of the whole reaction media, respectively. The heat produced locally by the highly exothermic reduction of SiO_2 by Mg (ΔH_r(1200 K) = -344 kJ mol^{-1} [42]) is expected to intensify the reactivity of Mg and to enhance the reaction rate, in a scenario close to a combustion synthesis.[48,49] The β-$FeSi_2$ concentration strongly increases (+23 %) between 873 K and 1173 K which is mostly attributed to the solid-state reaction between Fe (-17 %) and Si (-30 %).

At 1173 K, the reaction media is composed of β-$FeSi_2$, FeSi, Mg_2Si and some unreacted Si and Fe giving an overall Si/Fe metal ratio of 1.8. This is higher than the 1.5 ratio determined for the precursor mixture but still lower than the expected value of 2. This suggests that the reduction of amorphous SiO_2 is not yet completed at the end of the heating ramp. As indicated by the decrease of Mg_2Si content and the increase of Si/Fe ratio during the isothermal plateau, amorphous SiO_2 is slowly reduced by highly reactive Mg_2Si [50,51] according to the reaction:

$$SiO_2 + Mg_2Si \xrightarrow{1173\,K} 2\,Si + 2\,MgO \qquad \Delta G_r(1200\ K) = \text{-}252.0\ kJ\ [42]$$

Finally, after 10 h at 1173 K, XRD pattern shows that MgO and β-$FeSi_2$ are the main phases in the reduced pellets with only small amounts of residual Si and FeSi.

Weighing the pellets before the reaction and the powders after HCl-washing indicates reaction yields typically higher than 98 % using this process.

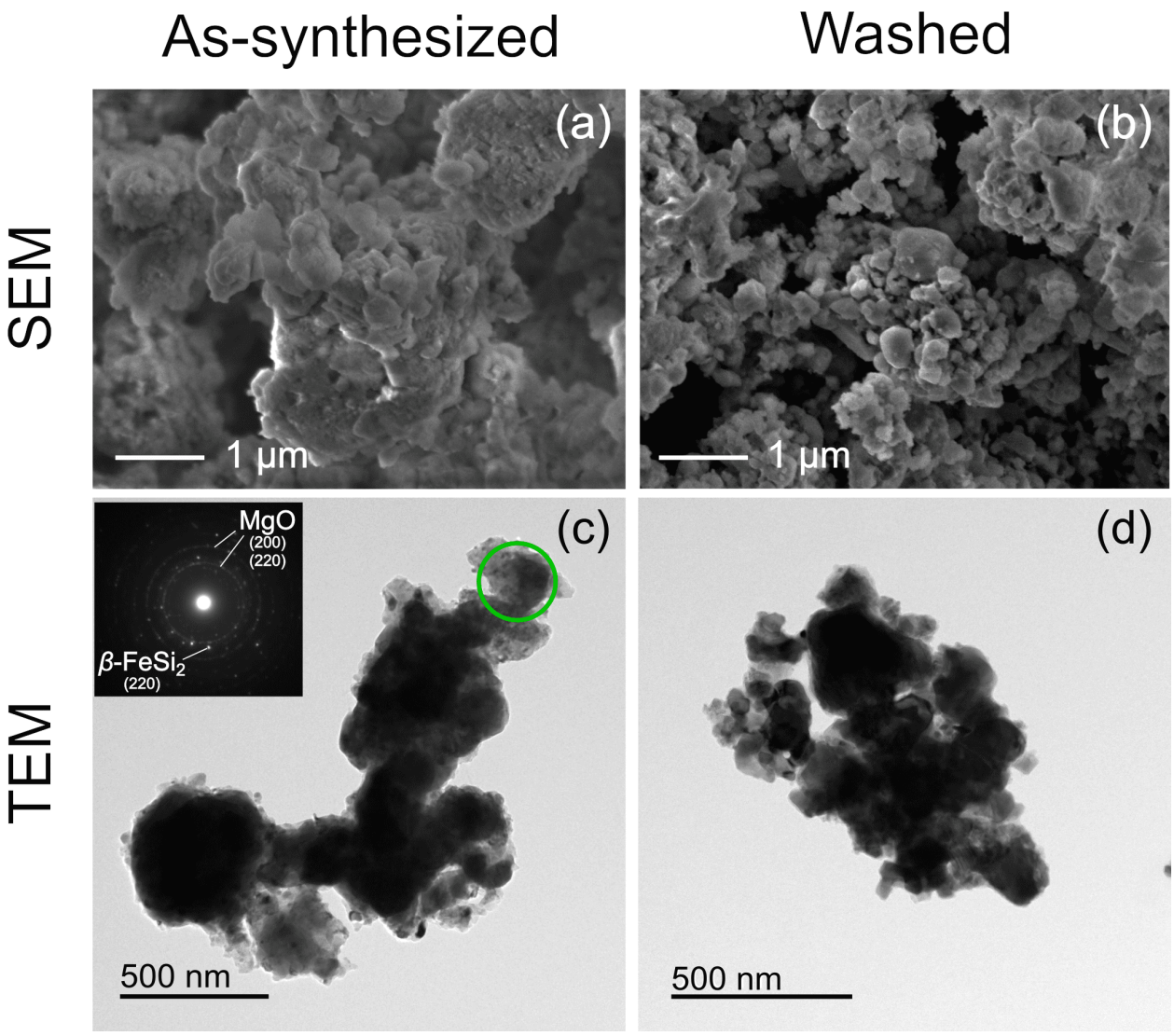

Figure 3: (a-b) Secondary electron SEM and (c-d) brightfield TEM images of the as-synthesized (left) and HCl-washed (right) MR β-$FeSi_2$ powder. The electron diffraction pattern shown in inset was taken at the green circle in (c).

MR-powder microstructure

SEM images of the as-synthesized MR β-$FeSi_2$ powder (fig. 3a) reveal aggregated particles with sizes below 400 nm. SEM-EDS elementary analyses confirm the Si/Fe metal ratio of 2 and the presence of Mg (60 at.%) ascribed to MgO. Typical TEM brightfield image of an aggregate is shown in fig. 3c. According to TEM-EDS analyses, the large darker areas at the center are mostly composed of Fe and Si while the surrounding brighter area corresponds to MgO. In addition, electron diffraction pattern in fig. 3c shows diffuse rings corresponding

to MgO (s.g. $Fm\bar{3}m$, a = 4.21 Å)[52] while sharp spots are ascribed to β-$FeSi_2$.[41] In light of these observations, the aggregate irregular shape of as-synthesized powder derives from the association of well-crystallized β-$FeSi_2$ particles (darker areas) being embedded inside a nanocrystalline MgO matrix (bright area). We hypothesize here that the MgO layer surrounding the β-$FeSi_2$ grains plays a significant role during the heat treatment to limit the grain growth and stabilize the submicronic size of the silicide.

After diluted hydrochloric acid washing, the diffraction peaks of MgO disappear on the XRD patterns, indicating its elimination at least below the detection level of the technique (fig. 1). The almost entire dissolution of MgO, as well as the homogeneous insertion of cobalt in the doped samples, are confirmed by SEM/TEM-EDS analyses.

Removal of the MgO layer reveals the morphology of the β-$FeSi_2$ particles (fig. 3b,d) having sizes spanning from 30 nm to about 400 nm, suggesting that the present magnesioreduction process produces powders with a slightly larger average size than the process described by Sen *et al.*[33] We attribute it to the smaller size of the oxide particles, lower reaction temperature (-100 K) and presence of MgO diluent in their precursor mixture. In our case, adding MgO diluent was found to considerably reduce the reaction kinetics.

3.2 Crystal structure

As reported by Dusausoy *et al.*,[41] β-$FeSi_2$ crystallizes in the orthorhombic *Cmce* space group with lattice parameters a = 9.8774(3) Å, b = 7.8128(3) Å and c = 7.8272(3) Å. This structure type derives from the fluorite-type structure by strongly distorting the [Si_8] cubes into irregular prisms where Fe-atoms occupy alternatively one half of the central sites (fig. 4a,b). In this initial description of the crystal structure, two independent Fe-sites are distributed over two kind of layers stacked along the a-axis (fig. 4a): the layer 1 contains the Fe1 atoms in *8d* Wyckoff site surrounded by [Si_8] trapezoid-based prisms, the layer 2 contains the Fe2 atoms in *8f* Wyckoff site coordinated by similar [Si_8] trapezoid-based prisms with additional torsion angle between the rectangular faces. This structure of β-$FeSi_2$ can also

be alternatively described as another layered one with ABAB stacking mode along the [100] direction, as shown in fig. 4a. While the individual layers are structurally identical, the layer A transforms into the layer B by the translation vector $x + 1/2$, $y + 1/2$, z, as represented in the projections along the a-axis of the layers in fig. 4c. In this description, each layer is composed of the layer 1 (fig. 4b) sandwiched between two half of the layer 2, and the pseudo-cubic layer 2 is build from the interaction of the A and B layers.

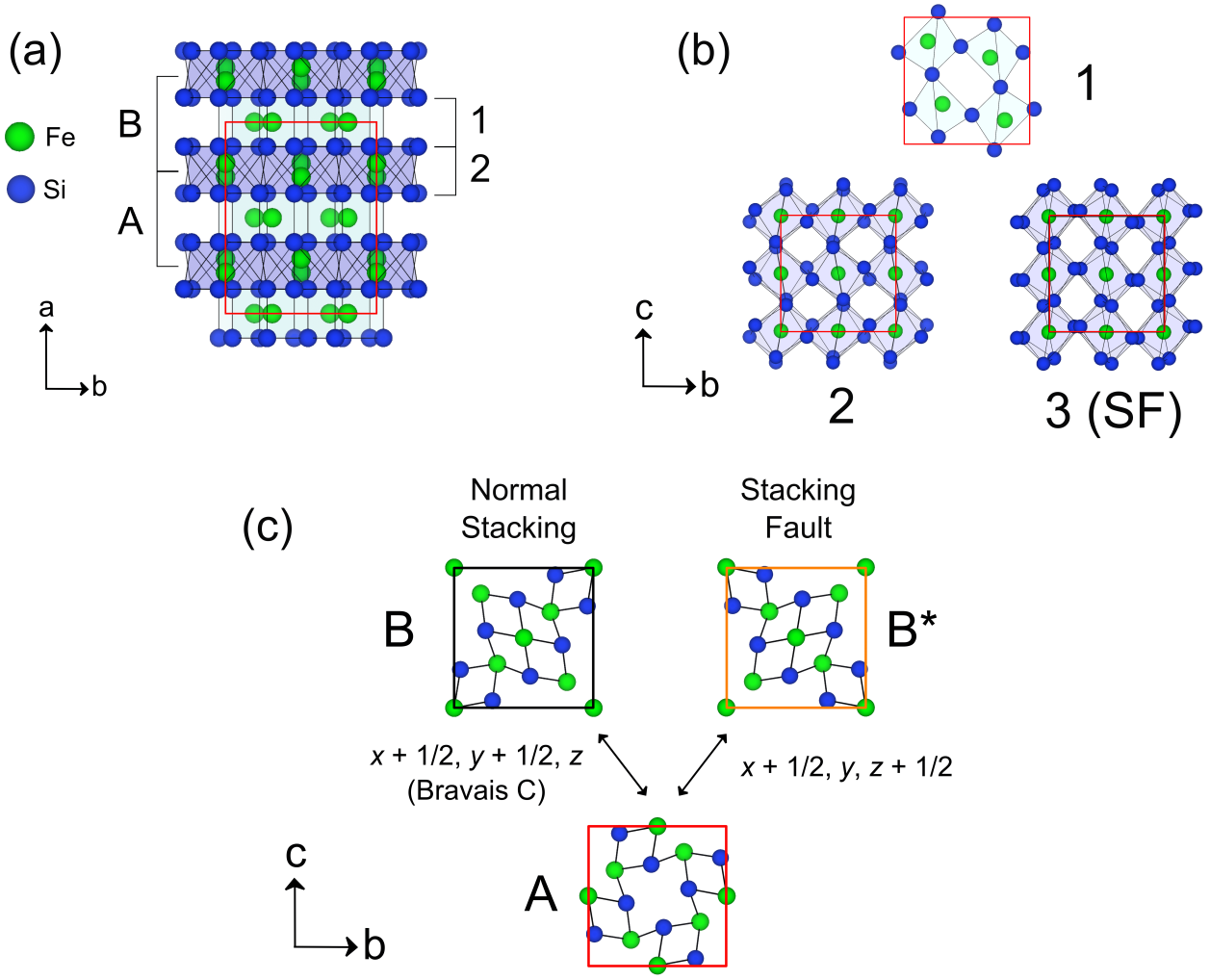

Figure 4: (a) c-axis projection of the crystal structure of β-$FeSi_2$ reported by Dusausoy *et al.*[41] showing the Fe@[Si_8] networks and the ABAB stacking mode; (b) a-axis projections of the pseudo-cubic networks 1, 2 and 3; (c) a-axis projections of the normal stacking A and B layers and alternative stacking layer B* along with related displacement vectors.

However, β-$FeSi_2$ is known to accommodate high concentration of intrinsic stacking faults

with displacement vector (100)[011]/2 as reported by Zheng *et al.*[53] and confirmed by Yamane *et al.*[54] In other words, the expected AB stacking is randomly replaced by an AB* one where the B* layer is obtained by a x+1/2, y, z+1/2 translation of the A-layer (fig. 4c). A consequence of these stacking faults is the formation of a third type of Fe@[Si_8] network (layer 3 in fig. 4b) at the interface of the stacking fault, which can be considered as a twinned version of the layer 2,[53] with minor differences in the Fe-atom coordination sphere.

In the case of the magnesioreduced powders, the presence of the stacking faults (SF) is highlighted by an important XRD peak shape broadening of the *hkl* reflections with $k+l \neq 2n$ (fig. 1) corresponding to diffuse streaks observed in the electron diffraction pattern along the a^*-direction for this condition (fig. 5a). Dark-field images obtained from the diffuse streaks of a crystal oriented along the $[0\bar{1}2]$ zone axis (fig. 5b) clearly reveal a high density of planar defects. High resolution TEM image of this defective crystal (fig. 5c) shows 4.9 Å *(i.e.* $a/2$) thick layers perpendicular to the [100] direction and AB or AB* stacking.

As pointed out by Yamane *et al.*,[54] the density of SF in β-$FeSi_2$ is strongly dependent on the synthesis method. Indeed, pulverized crystals grown in relatively mild conditions, *e.g.* metal flux or chemical transport methods, are found to be relatively free of SF while polycrystalline samples prepared for example by conventional fusion/solidification or powder metallurgical methods are more affected. In order to quantify the probability of SF in our samples, the general recursion method for crystals containing planar faults developped by Treacy *et al.*[39] has been applied to both pristine and Co-doped β-$FeSi_2$ prepared by magnesioreduction.

The SF have been taken into account in the modeling of the X-ray diffraction data using the dedicated FAULTS software.[38] For this, half a unit cell along the a-axis, corresponding to a single layer A (fig. 4), was considered along with two possible displacement vectors, $x + 1$, $y + 1/2$, z and $x + 1$, y, $z+ 1/2$ corresponding to the normal and faulty stacking, respectively. Using this approach, the patterns were refined by optimizing the stacking fault probability, the lattice and atomic parameters and the peak profile function. Refined

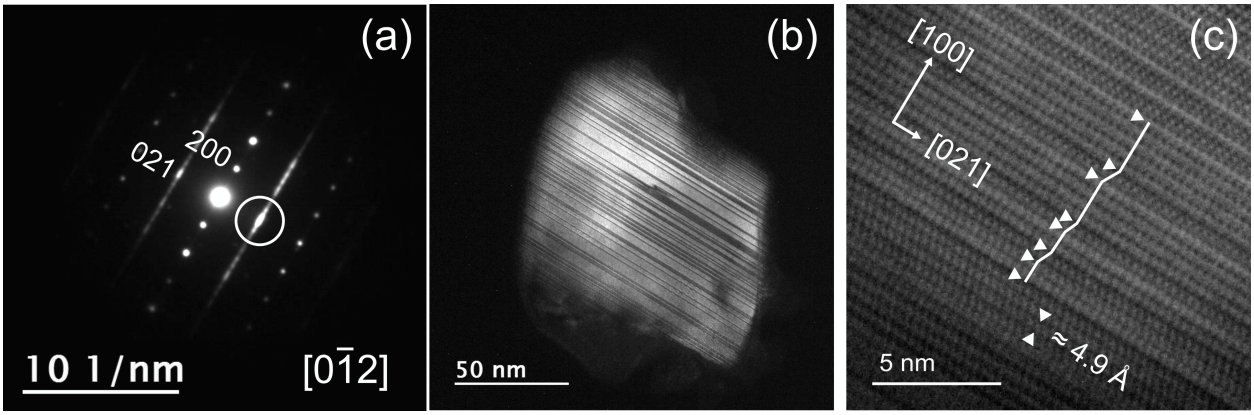

Figure 5: (a) Electron diffraction pattern of MR β-$FeSi_2$ taken along the [0$\bar{1}$2] zone axis showing diffuse streaks for *hkl* reflections with $k+l \neq 2n$. (b) Dark-field image using the diffuse streak (white circle) revealing high density of planar defects in MR $FeSi_2$(c) HRTEM image showing the stacking faults indicated with white arrows.

XRD patterns are shown in fig. 6 and refined structural parameters summarized in table 1. The atomic coordinates remain almost unchanged compared to Dusausoy's structural model and the atomic displacement parameters have regular values for intermetallic compounds. The SF probabilities were found to be close to 15 % for both compositions. This value is similar to the ratios reported by Yamane *et al.* for β-$FeSi_2$ samples synthesized by powder metallurgy methods.[54] As pointed out by Zheng *et al.*,[53] the layer 3 exhibits a twin-like structure, as if the b and c axes were exchanged in the defect layer. Thus with increasing the SF concentration, one expects the b and c lattice parameters to converge to an average value between those in the regular lattice. Accordingly, the b and c lattice parameters in the MR powders are rather close from each other. Interestingly, the lattice constant a of the Co-doped sample increasing from 9.88240(2) Å to 9.89838(8) Å seems to be the only structural parameter affected by the insertion of Co in the structure. This is consistent with Hesse*'s* work[55] reporting a linear increase of a with increasing Co substitution and an expected value of about $a = 9.905$ Å for β-$Co_{0.07}Fe_{0.93}Si_2$.

Table 1: Lattice parameters, atomic coordinates, isotropic thermal displacement parameters and stacking fault propability (SF) extracted from the Rietveld refinement of the HCl-washed MR β-$FeSi_2$ and MR β-$Co_{0.07}Fe_{0.93}Si_2$ XRD patterns

		MR β-$FeSi_2$	MR β-$Co_{0.07}Fe_{0.93}Si_2$
	a (Å)	9.88240(2)	9.89838(8)
	b (Å)	7.81651(2)	7.81778(8)
	c (Å)	7.83428(2)	7.82839(8)
	x	0.129(1)	0.128(1)
Si ($16g$)	y	0.273(1)	0.276(1)
	z	0.049(1)	0.045(1)
	x	0.124(1)	0.124(1)
Si ($16g$)	y	0.049(1)	0.046(1)
	z	0.272(1)	0.273(1)
	B_{iso} (Å^2)	0.4(1)	0.2(1)
Fe2 ($8f$)	y	0.309(1)	0.310(1)
	z	0.312(1)	0.310(1)
Fe1 ($8d$)	x	0.216(1)	0.216(1)
	B_{iso} (Å^2)	0.2(1)	0.1(1)
	SF (%)	14.8(1)	18.5(3)

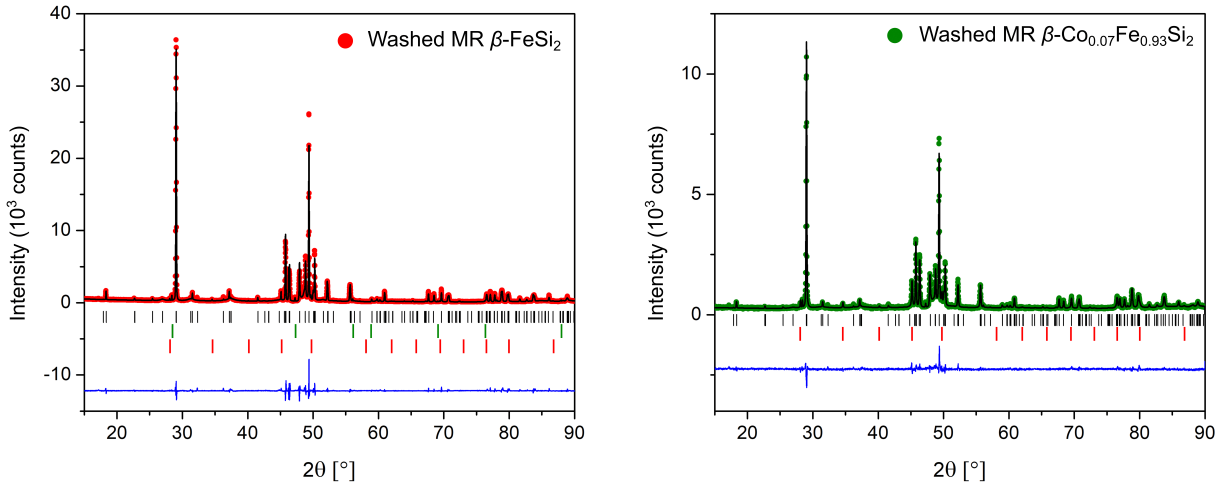

Figure 6: Rietveld refinement of the washed MR β-$FeSi_2$ (left) and MR β-$Co_{0.07}Fe_{0.93}Si_2$ (right) powder XRD. The experimental data are plotted in colored symbols, the calculated one with a black line and the difference with a blue line. The vertical ticks indicate the Bragg peak positions for β-$FeSi_2$ (black), FeSi (red) and Si (green).

3.3 Densified pellet microstructure

Any attempts to obtain densified pellets by spark plasma sintering below the decomposition temperature of β-$FeSi_2$ resulted in materials with low relative density (< 85 %) and were consequently abandoned. Pellets with 94 % and 97 % relative density were prepared from magnesioreduced (MR) and arc-melted (AM), respectively, β-$FeSi_2$ and β-$Co_{0.07}Fe_{0.93}Si_2$ powders by SPS at 1323 K followed by 24 h annealing at 1100 K to recover the expected β-phase. Backscattered electron SEM images and EDS mappings of polished pellet surfaces obtained from the MR process reveal relatively homogeneous chemical composition (fig. 7) with the exception of small amount of FeSi impurity as well as a few WSi_2 particles certainly coming from WC contamination during the early precursor milling. SEM-EDS elementary analyses realized on the Co-doped samples synthesized by MR or conventional AM routes give a similar global Co concentration of about 2 at.% in good agreement with the targeted composition. None of EDS spectra measured inside the grains show the presence of magnesium, indicating the absence of significant contamination of the silicides by this element.

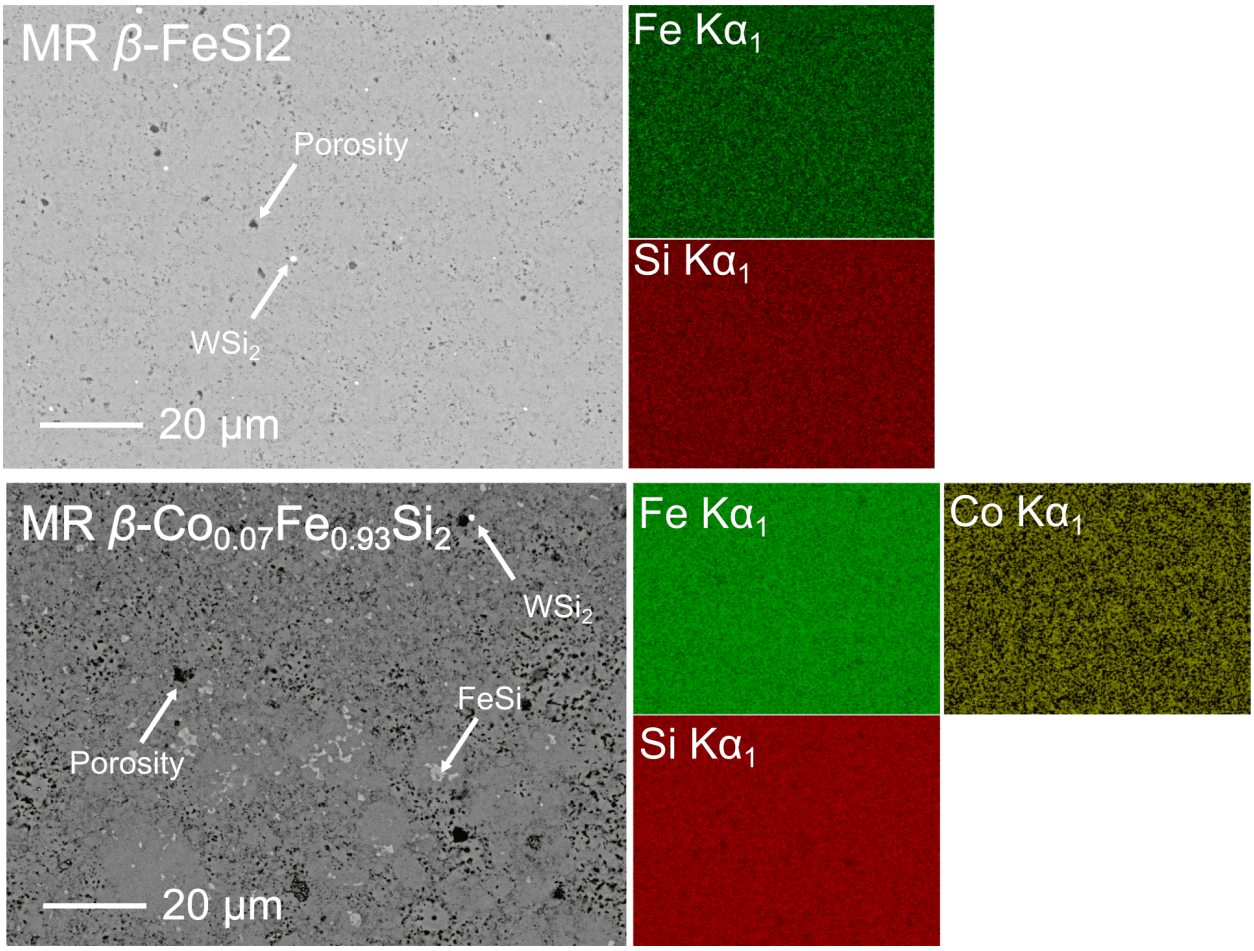

Figure 7: Backscattered electron SEM images and corresponding EDS mappings of the polished surface of undoped MR β-$FeSi_2$ (top) and MR β-$Co_{0.07}Fe_{0.93}Si_2$ (bottom) densified pellets.

Secondary electrons SEM images of the broken cross-section of undoped β-$FeSi_2$ densified pellets are shown in fig. 8 for MR and AM samples. The microstructure of the AM sample is relatively common for sintered iron silicides prepared by fusion-solidification techniques[15,18] and the particle sizes span from 1 μm to tens of μm. Porosity is hardly visible and only a few submicronic pores can be detected at high magnification in agreement with the high density (97 %) measured by the Archimede method. In the case of the MR samples, the microstructure is significantly different with less well-faceted particles and smaller average grain size (mainly from 500 nm to 1 μm range). By analogy with our previous report on higher manganese silicides and TEM analysis (fig. 3d) prior to SPS, we assume here that

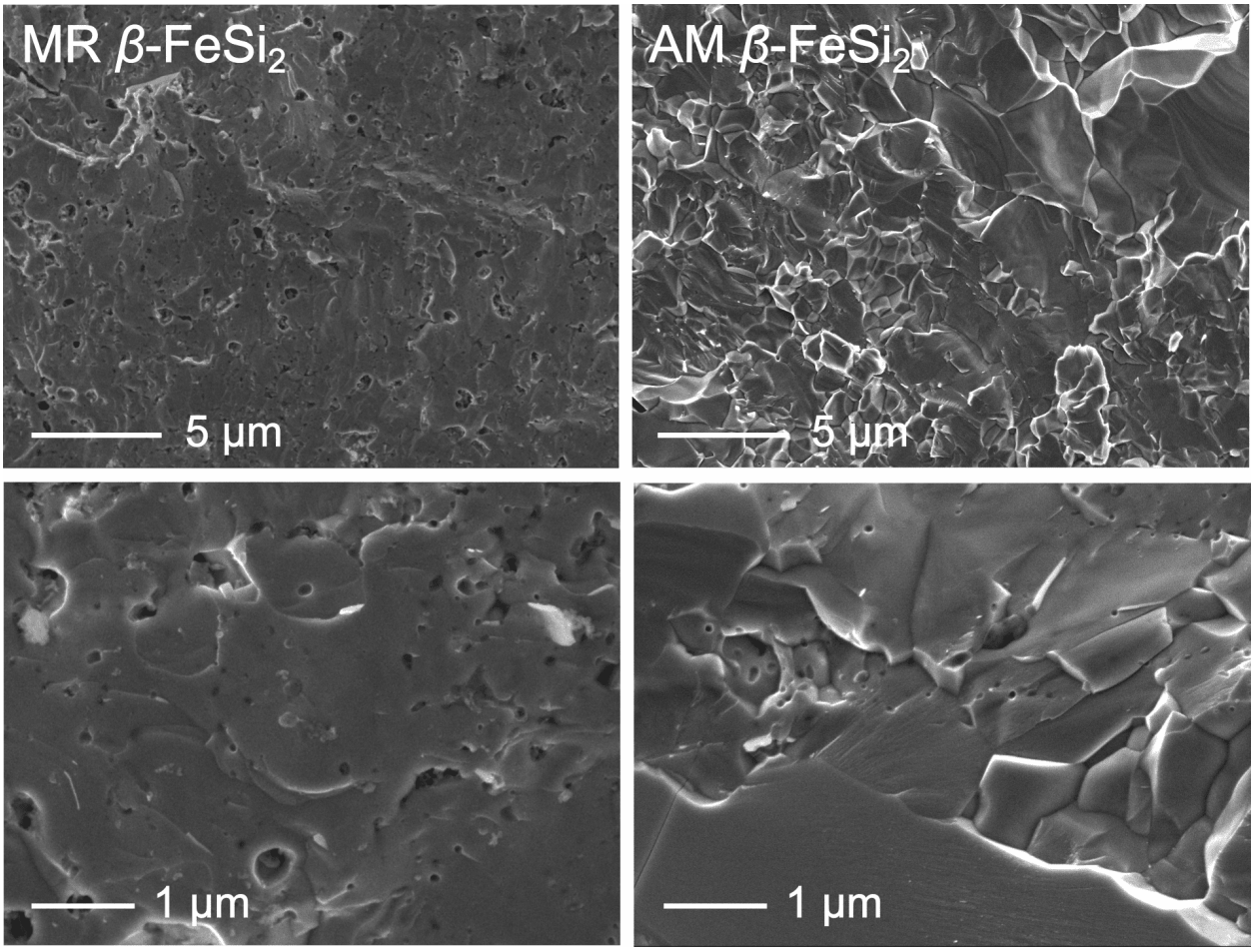

Figure 8: Secondary electron SEM images of broken cross-sections of MR (left side) and AM $FeSi_2$ (right side) at two different magnifications.

these MR particles are single crystals. As a consequence of the submicronic grain sizes, numerous residual porosities with sizes from 500 nm down to few tens of nanometers are observed for MR samples which is consistent with the larger deviation from full densification (94 %).

XRD realized on crushed pellets are presented in fig. 9a for undoped and in fig. S3 for Co-doped samples. Lattice and structural parameters extracted by refinements are presented in table 2 and table S10. The lattice constants and atomic coordinates are comparable for the corresponding compositions. More particularly, the similar a parameters for the doped samples suggest equivalent Co substitution in agreement with SEM-EDS results. The SF probability is however systematically higher for MR ($\approx$ 10 %) than for AM samples ($\approx$ 3 %).

The density of SF in the samples can be directly appreciated by comparison of the (312) Bragg reflections (fig. 9b) which become significantly less intense and broader with increasing SF probability. This result confirms that the synthesis route has a strong influence on the SF density in β-$FeSi_2$ even after high-temperature sintering/annealing steps.

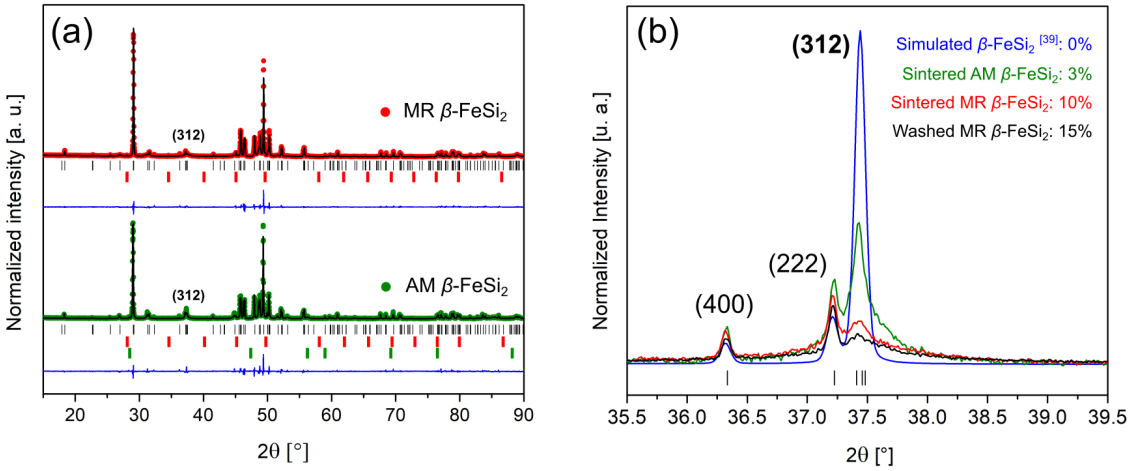

Figure 9: (a) FAULTS refined powder XRD patterns of sintered MR β-$FeSi_2$ (red) and AM β-$FeSi_2$ (green). The experimental data are plotted in colored symbols, the calculated one with a black line and the difference with a blue line. The vertical ticks indicate the Bragg peak positions for β-$FeSi_2$ (black), FeSi (red) and Si (green). (b) Influence of the stacking fault density on the (312) diffraction peak profile and intensity.

Table 2: Lattice parameters, stacking fault probability and impurity content for spark plasma sintered MR $FeSi_2$, AM $FeSi_2$, MR $Co_{0.07}Fe_{0.93}Si_2$, and AM $Co_{0.07}Fe_{0.93}Si_2$ obtained by refinements, together with their relative density obtained by the Archimede method.

	MR $FeSi_2$	AM $FeSi_2$	MR $Co_{0.07}Fe_{0.93}Si_2$	AM $Co_{0.07}Fe_{0.93}Si_2$
a (Å)	9.89104(6)	9.87518(4)	9.91176(8)	9.91200(4)
b (Å)	7.81612(3)	7.79980(3)	7.81410(4)	7.81500(4)
c (Å)	7.84209(3)	7.83727(2)	7.84084(5)	7.84060(3)
SF (%)	10.7(2)	3.7(1)	10.4(1)	3.2(1)
Rel. density (%)	94	97	94	97
Impurities (wt.%)	1 (FeSi)	1 (FeSi) 2.5 (Si)	2 (FeSi)	5 (FeSi)

Despite the phase transition from β-$FeSi_2$ to α-$Fe_{1-\delta}Si_2$ during the sintering process

and back to β-form after annealing, the microstructures of the densified materials remain significantly different for the two synthesis routes. The MR samples are characterized by smaller average particle sizes and higher density of grain boundaries, of porosities and higher concentration of SF. All these defects acting at different scales in the materials are expected to scatter efficiently the phonons over a broad energy spectrum and thus to reduce the thermal conductivity of $FeSi_2$. The influence of this microstructure on the thermoelectric properties of this material is thus presented in the following.

3.4 Thermoelectric properties

The TE properties of β-$FeSi_2$ and β-$Co_{0.07}Fe_{0.93}Si_2$ synthesized by magnesioreduction and arc-melting were investigated from room temperature up to 773 K. Measurements of the electronic properties were cycled twice and showed good reversibility. Undoped MR β-$FeSi_2$ samples have elevated electrical resistivity (14 mΩ m) (fig. 10a) and Seebeck coefficient (550 μV K^{-1}) (fig. 10b) at room temperature which is in agreement with the relatively low charge carrier concentration (10^{17} - 10^{18} cm^{-3}) reported for this semiconductor.[56,57] Interestingly, the Seebeck coefficients are positive for MR and negative for AM samples indicating n-type and p-type conductions, respectively. Experimental data from the literature report p-type[58] as well as n-type[14,27] bulk materials. The conduction type change is often attributed to the presence of impurities or defects (*e.g.* Fe or Si vacancies), which strongly depends on the synthesis route.[59] For instance Chu *et al.* also reported a change from p- to n-type conduction on a β-$FeSi_2$ thin film after prolonged annealing at 1163 K.[60] These results suggest that the synthesis routes, as well as the high-temperature treatment, can strongly influence the transport properties of β-$FeSi_2$ materials and possibly explain the different conduction types measured in the present work. Due to its smaller electrical resistivity and despite its smaller Seebeck coefficient, the *PF* of the MR β-$FeSi_2$ sample is found far superior to that of the AM sample on the whole temperature range, reaching a maximum value of 0.2 mW m^{-1} K^{-2} at 650 K (fig. 10c).

Upon Co doping, the electrical resistivities of both MR and AM samples significantly drop while the Seebeck coefficient stabilizes around -180 μV K^{-1}. This can be explained by the creation of donor levels in the band gap[61] increasing the estimated charge carriers concentration up to 10^{20} - 10^{21} cm^{-3} according to literature data.[58,62,63] The electrical resistivity of the MR sample is however systematically 35 % higher than the AM sample on the whole temperature range which can be partially explained by the lower density of the MR material.[16] The resulting *PF* are increased to values as high as 0.9 and 1.0 mW m^{-1} K^{-2} at 773 K for the MR and AM β-$Co_{0.07}Fe_{0.93}Si_2$, respectively.

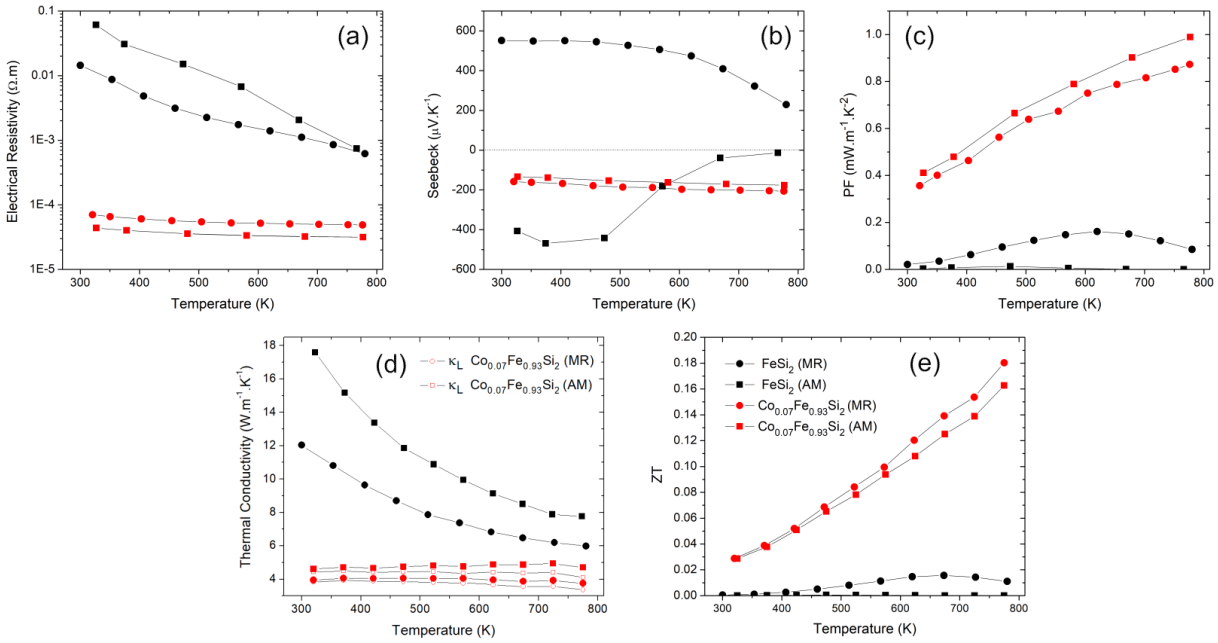

Figure 10: High temperature thermoelectric properties of β-$FeSi_2$ (black symbols) and β-$Co_{0.07}Fe_{0.93}Si_2$ (red symbols) synthesized by magnesioreduction (MR, circles) and conventional arc-melting (AM, squares). Thermal dependence of (a) the electrical resistivity, (b) the thermopower, (c) the power factor (*PF*), (d) the total (filled symbols) and lattice (empty symbols) thermal conductivity and (e) resulting figure-of-merit *ZT*.

The thermal conductivities of AM β-$FeSi_2$ and β-$Co_{0.07}Fe_{0.93}Si_2$ (fig. 10d) equal 17.5 and 4.7 W m^{-1} K^{-1} at room temperature, which is in good agreement with most literature data.[14,15,55,58] The lower thermal conductivity of the doped sample can be attributed to the mass fluctuation phenomenon at the mixed Fe/Co sites or to the scattering of phonons by polarons in these silicides.[58] The thermal conductivities of the respective MR synthesized

samples are comparatively lower by 32 % and 15 % at 320 K. At the highest temperature, the thermal conductivity reduction reaches 23 % for both compositions. The lattice thermal conductivity of all the samples were estimated by subtraction of κ_E calculated with the Wiedermann-Franz law $\kappa_e(T) = \mathrm{L}\cdot\mathrm{T}/\rho(T)$ with the commonly used $\mathrm{L} = 2.4.10^{-8}$ W Ω K^{-2} to the total thermal conductivity. The lower κ measured for MR samples can thus be mostly attributed to κ_L reduction reaching 24 % and 17 % at 773 K for the undoped and Co-doped sample, respectively. The MR and AM samples have similar compositions, so the reduction of κ_L is attributed to enhanced scattering at pores, grain boundaries and stacking faults,[64] all of which occur in higher densities in the MR materials. Eventually, maximum figure-of-merit ZT of 0.015 at 673 K and 0.18 at 773 K could be calculated for the undoped and doped MR samples, respectively (fig. 10e). In the case of MR β-$FeSi_2$, ZT has been improved compared to the AM sample mostly because of the reduced thermal conductivity, but it remains low due to the exceedingly large electrical resistivity. On the other hand, MR β-$Co_{0.07}Fe_{0.93}Si_2$ has a much higher maximum ZT, which corresponds to a 12 % improvement compared to the conventionally synthesized sample thanks to the mesostructuration. This value is to the best of our knowledge among the highest ZT value reported at this temperature for Co-doped β-$FeSi_2$.[15,65]

4 Conclusions

An optimized magnesioreduction synthesis of β-$FeSi_2$ and β-$Co_{0.07}Fe_{0.93}Si_2$ powders from (Co-doped) Fe_2O_3 and Si has been developed. It offers many advantages over more conventional synthesis routes such as the use of air-stable and inexpensive precursors, short heat treatment below the decomposition temperature of β-$FeSi_2$, very high yield (> 98 %) and a satisfying control of the chemical composition including dopant concentration. Detailed study of the reaction mechanism by means of XRD pattern Rietveld refinements enabled to determine the reduction starting temperature between 923 K and 973 K, the formation

of Mg_2Si intermediate during the process, and a total duration of the thermal treatment of 19 h to achieve a total reaction. After removal of MgO by-product by diluted HCl washing, the as-synthesized silicide powders are composed of well-crystallized grains with sizes ranging between 30 and 400 nm. TEM observations reveal high concentration of stacking faults evaluated at 15 - 18 % by refinement of the XRD pattern using a dedicated software. The high temperature TE properties of MR/SPS/annealed densified pellets were measured up to 773 K and compared to conventionally AM/SPS/annealed samples with similar compositions. The higher densities of grain boundaries, stacking faults and porosities in the magnesioreduced materials lead to strongly reduced lattice thermal conductivities. As a result, the TE figures-of-merit ZT of the two compositions are improved, even reaching 0.18 at 773 K in the case of β-$Co_{0.07}Fe_{0.93}Si_2$.

5 Conflicts of interest

There are no conflicts to declare.

Acknowledgement

The authors thank Loic Joanny and Francis Gouttefangeas for SEM images, and EDS analyses performed on the CMEBA platform. The TEM analyses were performed at THEMIS platform. Both platforms belong to the ScanMAT unit (UMS 2001, University of Rennes 1) which received a financial support from the European Union (CPER-FEDER 2007-2014). The authors acknowledge support from CREST JPMJCR15Q6 and JSPS KAKENHI JP17H02749, JP16H06441.

Supporting Information Available

- Figure SI 1: Le Bail refined XRD pattern of the $Co_{0.14}Fe_{1.86}O_3$ precursor;

- Figure SI 2: Rietveld refined XRD patterns of the samples at various stages of the reaction;
- Tables SI 1-9: Tables summarizing the refined parameters obtained from the refined patterns shown in figure SI 2;
- Figure SI 3: FAULTS refined XRD patterns of the sintered MR and AM β-$Co_{0.07}Fe_{0.93}Si_2$ samples;
- Table SI 10: Summary of the refined parameters obtained for the sintered β-$FeSi_2$ and β-$Co_{0.07}Fe_{0.93}Si_2$ XRD patterns synthesized from MR and AM routes.

References

(1) Bell, L. E. Cooling, Heating, Generating Power, and Recovering Waste Heat with Thermoelectric Systems. *Science* **2008**, *321*, 1457–1461.

(2) Petsagkourakis, I.; Tybrandt, K.; Crispin, X.; Ohkubo, I.; Satoh, N.; Mori, T. Thermoelectric materials and applications for energy harvesting power generation. *Sci. Technol. Adv. Mater* **2018**, *19*, 836–862.

(3) Pei, Y.; Wang, H.; Snyder, G. J. Band Engineering of Thermoelectric Materials. *Adv. Mater.* **2012**, *24*, 6125–6135.

(4) Yang, L.; Chen, Z.-G.; Dargusch, M. S.; Zou, J. High Performance Thermoelectric Materials: Progress and Their Applications. *Adv. Energy Mater.* **2018**, *8*, 1701797.

(5) Pei, Y.; Tan, G.; Feng, D.; Zheng, L.; Tan, Q.; Xie, X.; Gong, S.; Chen, Y.; Li, J.-F.; He, J.; Kanatzidis, M. G.; Zhao, L.-D. Integrating Band Structure Engineering with All-Scale Hierarchical Structuring for High Thermoelectric Performance in PbTe System. *Adv. Energy Mater.* **2017**, *7*, 1601450.

(6) Mori, T. Novel principles and nanostructuring methods for enhanced thermoelectrics. *Small* **2017**, *13*, 1702013.

(7) Luo, Z.-Z.; Zhang, X.; Hua, X.; Tan, G.; Bailey, T. P.; Xu, J.; Uher, C.; Wolverton, C.; Dravid, V. P.; Yan, Q.; Kanatzidis, M. G. High Thermoelectric Performance in Supersaturated Solid Solutions and Nanostructured n-Type PbTe-GeTe. *Adv. Funct. Mater.* **2018**, *28*, 1801617.

(8) Rogl, G.; Bursik, J.; Grytsiv, A.; Puchegger, S.; Soprunyuk, V.; Schranz, W.; Yan, X.; Bauer, E.; Rogl, P. Nanostructuring as a tool to adjust thermal expansion in high ZT skutterudites. *Acta Mater.* **2018**, *145*, 359–368.

(9) Hu, L.; Zhang, Y.; Wu, H.; Liu, Y.; Li, J.; He, J.; Ao, W.; Liu, F.; Pennycook, S. J.; Zeng, X. Synergistic Compositional-Mechanical-Thermal Effects Leading to a Record High ZT in n-Type V_2VI_3 Alloys Through Progressive Hot Deformation. *Adv. Funct. Mater.* **2018**, *28*, 1803617.

(10) Dolyniuk, J.-A.; Owens-Baird, B.; Wang, J.; Zaikina, J. V.; Kovnir, K. Clathrates Thermoelectrics. *Mater. Sci. Eng. R* **2016**, *108*, 1–46.

(11) Pei, Y.; Shi, X.; LaLonde, A.; Wang, H.; Chen, L.; Snyder, G. J. Convergence of electronic bands for high performance bulk thermoelectrics. *Nature* **2011**, *473*, 66–69.

(12) Shutoh, N.; Sakurada, S. Thermoelectric properties of the $Ti_x(Zr_{0.5}Hf_{0.5})_{1-x}NiSn$ half-Heusler compounds. *J. Alloys Compd* **2005**, *389*, 204–208.

(13) LeBlanc, S.; Yee, S. K.; Scullin, M. L.; Dames, C.; Goodson, K. E. Materials and manufacturing cost considerations for thermoelectrics. *Renew. Sust. Energ. Rev.* **2014**, *84*, 313–327.

(14) Kim, S.; Cho, M.; Mishima, Y.; Choi, D. High temperature thermoelectric properties of p- and n-type β-$FeSi_2$ with some dopants. *Intermetallics* **2003**, *11*, 399–405.

(15) He, Z.; Platzek, D.; Stiewe, C.; Chen, H.; Karpinski, G.; Müller, E. Thermoelectric properties of hot-pressed Al- and Co-doped iron disilicide materials. *J. Alloys Compd.* **2007**, *438*, 303–309.

(16) Gayner, C.; Prakash, D.; Ballal, A. Influence of secondary phases dispersants and porosity on thermoelectric properties of β-$Fe_{0.91}Mn_{0.09}Si_2$. *J. Alloys Compd.* **2017**, *698*, 164–169.

(17) Massalski, T. Binary Alloy Phase Diagrams. *Binary Alloy Phase Diagrams* **1990**,

(18) Qu, X.; Lü, S.; Hu, J.; Meng, Q. Microstructure and thermoelectric properties of β-$FeSi_2$ ceramics fabricated by hot-pressing and spark plasma sintering. *J. Alloys Compd.* **2011**, *509*, 10217–10221.

(19) Mohebali, M.; Liu, Y.; Tayebi, L.; Krasinski, J. S.; Vashaee, D. Thermoelectric figure of merit of bulk $FeSi_2$-$Si_{0.8}Ge_{0.2}$ nanocomposite and a comparison with β-$FeSi_2$. *Renew. Energ.* **2015**, *74*, 940–947.

(20) Poddar, V.; Dhokey, N.; Garbade, R.; Butee, S.; Prakash, D.; Purohit, R. Rapid production of Iron Disilicide thermoelectric material by Hot Press Sintering Route. *Mat. Sci. Semicon. Proc.* **2017**, *71*, 477–481.

(21) Han, L.; Xin-Feng, T.; Wei-Qiang, C.; Qing-Jie, Z. Quick preparation and thermal transport properties of nanostructured β-$FeSi_2$ bulk material. *Chinese Phys. B* **2009**, *18*, 287–923.

(22) Ail, U.; Gorsse, S.; Perumal, S.; Prakasam, M.; Umarji, A.; Vivs, S.; Bellanger, P.; Decourt, R. Thermal conductivity of β-$FeSi_2$/Si endogenous composites formed by the eutectoid decomposition of α-Fe_2Si_5. *J. Mater. Sci.* **2015**, *50*, 6713–6718.

(23) Liu, N.; Jensen, W. A.; Zebarjadi, M.; Floro, J. A. Tunable β-$FeSi_2$ - $Si_{1-y}Ge_y$ nanocom-

posites by a novel React/Transform Spark Plasma Sintering approach for thermoelectric applications. *Mater. Today Phys.* **2018**, *4*, 19–27.

(24) Jensen, W. A.; Liu, N.; Rosker, E.; Donovan, B. F.; Foley, B.; Hopkins, P. E.; Floro, J. A. Eutectoid transformations in Fe-Si Alloys for thermoelectric applications. *J. Alloys Compd.* **2017**, *721*, 705–711.

(25) Liu, N.; Rezaei, E.; Jensen, W. A.; Song, S.; Ren, Z.; Esfarjani, K.; Zebarjadi, M.; Floro, J. A. Improved thermoelectric performance of eco-friendly β-$FeSi_2$-SiGe nanocomposite via synergistic hierarchical structuring, phase percolation, and selective doping. *Adv. Funct. Mater.* **2019**, *29*, 1903157.

(26) Redzuan, F. L. B. M.; Mikio, I.; Masatoshi, T. Synthesis of Co-doped β-$FeSi_2$/Si composites through eutectoid decomposition and its thermoelectric properties. *J. Mater. Sci.* **2018**, *10*, 7683–7690.

(27) Rajasekar, P.; Umarji, A. M. Effect of Al-doping on suppression of thermal conductivity in Si dispersed β-$FeSi_2$. *Intermetallics* **2017**, *89*, 57–64.

(28) Parasuraman, R.; Wu, Y.; Ordonez-Miranda, J.; Volz, S.; Umarji, A. M. Particle size effect on the thermal conductivity reduction of silicon based thermoelectric composites. *Sustain. Energ. Fuels.* **2018**, *2*, 1764–1771.

(29) Redzuan, F. L. B. M.; Ito, M.; Takeda, M. Phosphorus doping in n-type β-$FeSi_2$/Si composites and its effects on thermoelectric properties. *Intermetallics* **2019**, *108*, 19–24.

(30) Wu, H.; Hu, B.; Tian, N.; Zheng, Q. Preparation of β-$FeSi_2$ thermoelectric material by laser sintering. *Mater. Lett.* **2011**, *65*, 2877–2879.

(31) Kinemuchi, Y.; Mikami, M.; Terasaki, I.; Shin, W. Rapid synthesis of thermoelectric compounds by laser melting. *Mater. Des.* **2016**, *106*, 30–36.

(32) Bywalez, R.; Orthner, H.; Mehmedovic, E.; Imlau, R.; Kovacs, A.; Luysberg, M.; Wiggers, H. Direct gas-phase synthesis of single-phase β-$FeSi_2$ nanoparticles. *J. Nanopart. Res.* **2013**, *15*, 1878.

(33) Sen, S.; Gogurla, N.; Banerji, P.; Guha, P. K.; Pramanik, P. Synthesis and characterization of β-phase iron silicide nano-particles by chemical reduction. *Mater. Sci. Eng. B* **2015**, *200*, 28–39.

(34) Sen, S.; Guha, P. K.; Banerji, P.; Pramanik, P. Mn and As doping of β-$FeSi_2$ via a chemical method. *RSC Adv.* **2016**, *6*, 68238.

(35) Le Tonquesse, S.; Alleno, E.; Demange, V.; Dorcet, V.; Joanny, L.; Prestipino, C.; Rouleau, O.; Pasturel, M. Innovative One-step Synthesis of Mesostructured $CoSb_3$-based Skutterudites by Magnesioreduction. *J. Alloys Compd.* **2019**, *796*, 176–184.

(36) Le Tonquesse, S.; Dorcet, V.; Joanny, L.; Demange, V.; Prestipino, C.; Guo, Q.; Berthebaud, D.; Mori, T.; Pasturel, M. Mesostructure - thermoelectric properties relationships in $V_xMnSi_{1.74}$ (x = 0, 0.04) Higher Manganese Silicides prepared by magnesiothermy. *J. Alloys Compd.* **2020**, 10.1016/j.jallcom.2019.152577.

(37) Pérez-Alonso, F. J.; Granados, M. L.; Ojeda, M.; Terreros, P.; Rojas, S.; Herranz, T.; Fierro, J. L. G.; Gracia, M.; Gancedo, J. R. Chemical structures of coprecipitated Fe-Ce mixed oxides. *Chem. Mater.* **2005**, *17*, 2329–2339.

(38) Casas-Cabanas, M.; Reynaud, M.; Rikarte, J.; Horbachb, P.; Rodriguez-Carvajal, J. FAULTS: a program for refinement of structures with extended defects. *J. Appl. Crystallogr.* **2016**, *49*, 2259–2269.

(39) Treacy, M. M. J.; Newsam, J. M.; Deem, M. W. A general recursion method for calculating diffracted intensities from crystals containing olanar faults. *Proc. R. Soc. London Ser. A* **1991**, *433*, 499–520.

(40) Rodriguez-Carvajal, J. Recent advances in magnetic-structure determination by neutron powder diffraction. *Physica B* **1993**, *192*, 55–69.

(41) Dusausoy, P.; Protas, J.; Wandji, R.; Roques, B. Crystal structure of iron disilicide, $FeSi_2\beta$. *Acta Crystallogr. B* **1971**, *27*, 1209–1218.

(42) Knacke, O.; Kubaschewski, O.; Hesselmann, K. *Thermo-chemical Properties of Inorganic Substances* **1991**,

(43) Wang, X.; Wang, S.; Hu, W.; Cai, J.; Zhang, L.; Dong, L.; Zhao, L.; He, Y. Synthesis and photocatalytic activity of SiO2/g-C3N4composite photocatalyst. *Mater. Lett.* **2014**, *115*, 53–56.

(44) Dézsi, I.; Fetzer, C.; Bujdosó, L.; Brötz, J.; Balogh, A. Mechanical alloying of Fe-Si and milling of α- and β-$FeSi_2$ bulk phases. *J. Alloys Compd.* **2010**, *508*, 51–54.

(45) Nagai, H. Effect of mechanical alloying and grinding on the preparation and thermoelectric properties of β-$FeSi_2$. *Mater. Trans., JIM* **1995**, *36*, 365–372.

(46) Toraya, H. Estimation of statistical uncertainties in quantitative phase analysis using the Rietveld method and the whole-powder-pattern decomposition method. *J. Appl. Crystallogr.* **2000**, *33*, 1324–1328.

(47) Haynes, W. H.; Lide, D. R.; Bruno, T. J. *CRC Handbook of Chemistry and Physics, 96^{th} Edition* **2015-2016**,

(48) Won, C.; Nersisyan, H.; Won, H. Titanium powder prepared by a rapid exothermic reaction. *Chem. Eng. J.* **2010**, *157*, 270–275.

(49) Nersisyan, H.; Won, H.; Won, C.; Joc, A.; Kim, J. Direct magnesiothermic reduction of titanium dioxide to titanium powder through combustion synthesis. *Chem Eng J* **2014**, *235*, 67–74.

(50) Xing, Z.; Lu, J.; Ji, X. A Brief Review of Metallothermic Reduction Reactions for Materials Preparation. *Small Methods* **2018**, *2*, 1800062.

(51) Haouli, S.; Boudebane, S.; Slipper, I. J.; Lemboub, S.; Gebara, P.; Mezrag, S. Combustion synthesis of silicon by magnesiothermic reduction. *Phosphorus Sulfur Silicon Relat. Elem.* **2018**, *193*, 280–287.

(52) Wechsler, B. A.; Navrotsky, A. Thermodynamics and structural chemistry of compounds in the system MgO-TiO_2. *J. Solid State Chem.* **1984**, *55*, 165–180.

(53) Zheng, Y.; Taccoen, A.; Petroff, J. F. Planar defects in β-iron disilicide (β-$FeSi_2$) analyzed by transmission electron-microscopy and modeling. *J. Appl. Crystallogr.* **1992**, *25*, 122–128.

(54) Yamane, H.; Yamada, T. Effect of stacking fault on the diffraction intensities of β-$FeSi_2$. *J. Alloys Compd.* **2009**, *476*, 282–287.

(55) Hesse, J.; Bucksch, R. Solid Solubility of $CoSi_2$ in β-$FeSi_2$. *J. Mater. Sci.* **1970**, *5*, 272–273.

(56) Arushanov, E.; Lisunov, K. G. Transport properties of β-$FeSi_2$. *Jpn. J. Appl. Phys.* **2015**, *54*, 07JA02.

(57) Arushanov, E.; Lange, H.; Werner, J. Hole Mobility in p-Type β-$FeSi_2$ Single Crystals. *Phys. Stat. Sol.* **1998**, *166*, 853–859.

(58) Tani, J.; Kido, H. Thermoelectric Properties of β-$Fe_{1-x}Co_xSi_2$ Semiconductors. *Jpn. J. Appl. Phys.* **2001**, *40*, 3236–3239.

(59) Tani, J.; Kido, H. First-principle study of native point defects in β-$FeSi_2$. *J. Alloys Compd* **2003**, *352*, 153–157.

(60) Chu, S.; Hirohada, T.; Kan, H. Room Temperature 1.58 μm Photoluminescence and Electric Properties of Highly Oriented β-$FeSi_2$ Films Prepared by Magnetron-Sputtering Deposition. *Jpn. J. Appl. Phys.* **2002**, *41*, L299–L301.

(61) Ware, R. M.; McNeill, D. J. Iron disilicide as a thermoelectric generator material. *Proc. IEE* **1964**, *111*, 178–182.

(62) Brehme, S.; Behr, G.; Heinrich, A. Electrical properties of Co-doped β-$FeSi_2$ crystals. *J. Appl. Phys.* **2001**, *89*, 3798–3803.

(63) Tani, J.; Kido, H. Electrical properties of Co-doped and Ni-doped β-$FeSi_2$. *J. Appl. Phys.* **1998**, *84*, 1408–1411.

(64) Lefévre, R.; Berthebaud, D.; Lebedev, O.; Pérez, O.; Castro, C.; Gascoin, S.; Chateigner, D.; Gascoin, F. Layered tellurides: stacking faults induce low thermal conductivity in the new $In_2Ge_2Te_6$ and thermoelectric properties of related compounds. *J. Mater. Chem. A* **2017**, *5*, 19406.

(65) Nozariasbmarz, A.; Agarwal, A.; Coutant, Z. A.; Hall, M. J.; Liu, J.; Liu, R.; Malhotra, A.; Norouzzadeh, P.; Öztürk, M. C.; Ramesh, V. P.; Sargolzaeiaval, Y.; Suarez, F.; Vashaee, D. Thermoelectric silicides: A review. *Jpn. J. Appl. Phys.* **2017**, *56*, 05DA04.

Graphical TOC Entry